

The effect of viscous relaxation on the spatiotemporal stability of capillary jets

Alejandro Sevilla

Área de Mecánica de Fluidos, Universidad Carlos III de Madrid, 28911 Leganés, Spain.

(Received xx; revised xx; accepted xx)

The linear spatiotemporal stability properties of axisymmetric laminar capillary jets with fully developed initial velocity profiles are studied for large values of both the Reynolds number, $Re = Q/(\pi a \nu)$, and the Froude number, $Fr = Q^2/(\pi^2 g a^5)$, where a is the injector radius, Q the volume flow rate, ν its kinematic viscosity, and g the gravitational acceleration. The downstream development of the basic flow and its stability are addressed with an approximate formulation that takes advantage of the jet slenderness. The base flow is seen to depend on two parameters, namely a Stokes number, $G = Re/Fr$, and a Weber number, $We = \rho Q^2/(\pi^2 \sigma a^3)$, where σ is the surface tension coefficient, while its linear stability depends also on the Reynolds number. When non-parallel terms are retained in the local stability problem, the analysis predicts a critical value of the Weber number, $We_c(G, Re)$, below which a pocket of local absolute instability exists within the near field of the jet. The function $We_c(Re)$ is computed for the buoyancy-free jet, showing marked differences with the results previously obtained with uniform velocity profiles. It is seen that, in accounting for gravity effects, it is more convenient to express the parametric dependence of the critical Weber number with use made of the Morton and Bond numbers, $Mo = \nu^4 \rho^3 g / \sigma^3$ and $Bo = \rho g a^2 / \sigma$, as replacements for G and Re . This alternative formulation is advantageous to describe jets of a given liquid for a known value of g , in that the resulting Morton number becomes constant, thereby leaving Bo as the only relevant parameter. The computed function $We_c(Bo)$ for a water jet under Earth gravity is shown to be consistent with the experimental results of Clanet & Lasheras (*J. Fluid Mech.* vol. 383, 1999, p. 307) for the transition from jetting to dripping of water jets discharging into air from long injection needles, which cannot be properly described with a uniform velocity profile assumed at the jet exit.

1. Introduction

The instability of capillary jets is a phenomenon of great importance in many applications like propulsion, irrigation, ink-jet printing and microfluidics (see the reviews Bogy 1979; Eggers 1997; Lin & Reitz 1998; Barrero & Loscertales 2007; Eggers & Villermaux 2008). One particular aspect of this flow which has received a lot of attention in the last decade, mainly due to its relevance in emerging microfluidic applications (see for instance Basaran 2002; Utada *et al.* 2007), is the fact that a minimum flow rate is required to achieve a *jetting regime*, in which droplets detach from the tip of a slender liquid column either due to the growth of capillary instabilities (Rayleigh 1878), or an end-pinching mechanism (Gordillo & Gekle 2010). In contrast, flow rates smaller than this minimum value give rise to a *dripping regime*, in which drop formation takes place directly at the injector outlet, providing comparatively larger drops at a smaller frequency (Wilkes *et al.* 1999; Ambravaneswaran *et al.* 2004). In the simplest situation, in which the effect of the outer fluid can be neglected, the existence of these two regimes can be explained in physical terms by a competition between the inertia of the liquid,

which promotes the formation of a slender jet, and the surface tension forces, which tend to destabilise it (see Eggers & Villermaux 2008). The relative importance of these forces is measured by a liquid Weber number, such that the dripping and jetting regimes prevail for values of the Weber number smaller and larger than certain critical values, respectively.

The fact that a slender capillary jet cannot be sustained for arbitrarily small values of the liquid Weber number was early recognised (see for instance Smith & Moss 1917). However, this *global* destabilisation phenomenon cannot be explained within the classical temporal stability analysis of Rayleigh (1878), and a theoretical explanation had to wait until the work of Leib & Goldstein (1986*b*), who found that a parallel capillary jet becomes absolutely unstable to inviscid axisymmetric perturbations for values of the Weber number below a certain critical value, which they found to depend on the specific shape of the axial velocity profile. Although these authors realised that “the double root in the present flow will be associated with some natural droplet formation process”, they did not identify the onset of absolute instability in the jet as responsible for the transition from jetting to dripping. In the case of jets with uniform velocity profiles, Leib & Goldstein (1986*a*) showed that the critical Weber number decreases as the Reynolds number decreases, indicating the stabilising effect of viscosity. The experiments of Monkewitz *et al.* (1988) led to the conjecture that the jetting-dripping transition could be due to the destabilization of a linear global mode in the sense of Chomaz *et al.* (1988). This possibility was investigated by Le Dizès (1997), who performed a stability analysis of the falling capillary jet with uniform velocity profile for large Reynolds and Froude numbers. Le Dizès (1997) found that a sufficiently long region of absolute instability near the orifice does indeed destabilise a linear global mode due to the interaction of three spatial branches of the dispersion relation. The corresponding critical value of the Weber number, computed by Le Dizès (1997) for Reynolds numbers between 100 and 200, was shown to be in good quantitative agreement with the experimental point of Monkewitz *et al.* (1988) for $Re \simeq 180$. It is interesting to note that the related configuration of a gas jet injected into stagnant liquid is absolutely unstable regardless of the value of the gas Weber number and, correspondingly, a bubbling regime is observed in experiments (Oğuz & Prosperetti 1993). However, a convective instability type is also possible in this system when a sufficiently fast liquid coflow is imposed, as shown by Sevilla *et al.* (2005), where the predictions of spatiotemporal stability theory were shown to be in good agreement with the experimental observation of the transition from a bubbling to a jetting regime.

A detailed experimental study of the jetting/dripping transition in water jets discharging from long needles was performed by Clanet & Lasheras (1999), where a successful mechanical model for the dripping to jetting transition was also developed. In particular, the experiments of Clanet & Lasheras (1999) revealed the presence of hysteresis in the dripping/jetting and jetting/dripping transitions when the injector diameter is sufficiently large. In dimensionless terms, hysteresis appears at high enough values of the Bond number, for which the critical Weber number for the dripping to jetting transition is substantially larger than the corresponding value for the reverse process. Moreover, Clanet & Lasheras (1999) found that the critical Weber number increases as the Bond number decreases, in qualitative, albeit not quantitative, agreement with the prediction of Le Dizès (1997). Moreover, the critical Weber number was found by Clanet & Lasheras (1999) to remain approximately constant for small enough values of the Bond number. Surprisingly, this limiting value of the critical Weber number is

closer to the theoretical result for the appearance of absolute instability in an *inviscid* jet with *uniform* velocity profile (Leib & Goldstein 1986*b*), than to the actual, expectedly more exact, prediction by Le Dizès (1997). A natural explanation for this discrepancy is that, while the theory of Le Dizès (1997) assumes a uniform velocity profile, the experiments of Clanet & Lasheras (1999) were performed with long needles for which the exit velocity profile is close to the fully-developed, parabolic Poiseuille profile. In fact, the analysis of Leib & Goldstein (1986*b*) contemplated the influence of the velocity profile shape by introducing the parametric family $(1 - br^2)/(1 - b/2)$, where r is the radial coordinate, and the parameter b was varied between 0 and 1, respectively corresponding to uniform and parabolic profiles. The latter was found to be more stable, having a critical Weber number approximately seven times smaller than the uniform one. Leib & Goldstein (1986*b*) suggested that their parametric profiles could be used to model the viscous relaxation process of a capillary jet with parabolic initial velocity profile, with the downstream position corresponding to a certain value of the parameter b . However, the actual shapes of the velocity profiles within the relaxation region are different from the parametric family proposed by Leib & Goldstein (1986*b*). Moreover, the relationship between the downstream position and the value of the parameter b is not uniquely defined.

The present work addresses the linear spatiotemporal stability properties of laminar capillary jets with fully-developed outlet velocity profiles, assuming large values of the Reynolds and Froude numbers in the analysis. In contrast with previous stability studies, which used parametric shapes to describe the downstream evolution of the jet velocity profiles, here the base flow is computed by integrating the axisymmetric boundary layer equations. The linear spatiotemporal stability of the resulting slender flow is then studied using a quasi-parallel approximation. The paper is organised as follows: first, in §2, we present the model considered for the base flow, as well as for the computation of its linear stability. Then, in §3, we present the results of the spatiotemporal stability analysis, and discuss its relationship with the phenomenon of transition to dripping observed in experiments. Finally, §4 is devoted to the conclusions.

2. Formulation of the problem

The configuration under study consists of a flow rate Q of liquid with density ρ and viscosity μ discharging downwards from a tube of radius a and length l_t into a stagnant atmosphere of gas of density ρ_g at pressure p_a . The tube wall is assumed vanishingly thin, so that a and l_t are the only relevant geometric length scales for the jet. Note that this formulation would also apply to tubes of finite thickness if the liquid does not wet the exit section, so that the contact line is pinned at the inner edge of the tube at its outlet. To describe the resulting liquid jet we will adopt a cylindrical coordinate system with its origin placed at the center of the exit section and the axial coordinate pointing in the direction of gravity, as depicted in figure 1. We shall assume values the Reynolds number such that $1 \ll Re = Q/(\pi a \nu) \lesssim 1000$, the latter limit in order to ensure laminar flow in the jet, as well as values of the Froude number $Fr = Q^2/(\pi^2 g a^5) \gg 1$, where g is the gravitational acceleration. Keeping in mind that jet formation requires values of the Weber number $We = \rho Q^2/(\pi^2 \sigma a^3) \gtrsim \mathcal{O}(1)$, and that $Re = We^{1/2}/Oh$, the first condition is fulfilled whenever the Ohnesorge number $Oh = \mu/(\rho \sigma a)^{1/2} \ll 1$, where σ is the surface tension coefficient. Notice that Oh does not depend on the jet velocity, and can be seen as a Reynolds number based on the capillary velocity, $(\sigma/(\rho a))^{1/2}$.

With these assumptions, the free laminar liquid jet which appears downstream of the

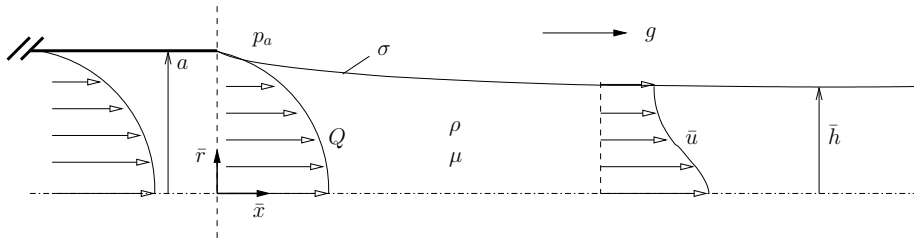


FIGURE 1. Sketch of the flow configuration considered in the present work at a given instant.

tube exit contracts due to the action of gravity, as well as to the viscous relaxation of the initial velocity profile, which is non-uniform at the injector exit due to the accumulated action of the viscous shear stress at the inner wall. The exact shape of this velocity profile depends on the detailed geometry of the injection system as well as on the Reynolds number, precluding a universal description of the resulting free jet. In this work we will consider the limiting case of a jet discharging from a long cylindrical tube with $l_t \gtrsim Re a \gg a$, such that the exit velocity profile is the fully-developed Poiseuille profile, $\bar{u}_0 = 2U_0(1 - \bar{r}^2/a^2)$, where $U_0 = Q/\pi a^2$ is the mean exit velocity. Throughout the text, quantities with bar will denote dimensional variables. Laminar liquid jets with fully developed velocity profiles at the outlet appear frequently in applications. In particular, this is the case of the experiments of Clanet & Lasheras (1999), devoted to the study of transition from dripping to jetting in water jets under Earth gravity. However, it is important to emphasise that the hypodermic needles used by Clanet & Lasheras (1999) had finite wall thickness, and the liquid wetted their entire exit section. Therefore, in those experiments the contact line was pinned at the *outer* edge and, consequently, the thin wall configuration considered in the present work cannot be considered fully equivalent to the flow experimentally studied by Clanet & Lasheras (1999). In particular, in contrast with the simplified boundary layer description used here, flow separation and recirculation are expected to take place in a small region near the needle exit section whenever the contact line is pinned at the outer edge. The structure of the flow in this region must be studied with the full Navier-Stokes equations, and is outside the scope of the present investigation. Keeping in mind the difference between both configurations, and in the absence of experimental data corresponding to the thin wall limit, the results of Clanet & Lasheras (1999) will be compared in §3.2 with those obtained in the present work.

As mentioned above, the streamwise contraction of the jet is due to a combined contribution of gravity and viscous relaxation. Concerning the former, the characteristic axial distance l_g over which gravity accelerates the jet by a quantity of the order of its initial velocity is given by a balance between the convective acceleration of the liquid, $\bar{u} \partial \bar{u} / \partial \bar{x} \sim U_0^2 / l_g$, and the gravitational acceleration, g , so that $l_g \sim Fr a$. On the other hand, viscous relaxation takes place within a distance l_r of the exit such that the convective acceleration U_0^2 / l_r balances the viscous diffusion term, of order $\nu U_0 / a^2$, giving $l_r \sim Re a$. From these considerations it is clear that the conditions $Fr \gg 1$, $Re \gg 1$ suffice to ensure the slenderness of the jet, whose downstream evolution will be described

here by means of the following decomposition,

$$\bar{u} = U_0 [U(X, r) + \epsilon u'(x, r, t)], \quad (2.1)$$

$$\bar{v} = U_0 [Re^{-1} V(X, r) + \epsilon v'(x, r, t)], \quad (2.2)$$

$$\bar{p} = \rho U_0^2 [P(X, r) + \epsilon p'(x, r, t)], \quad (2.3)$$

$$\bar{h} = a [H(X) + \epsilon h'(x, t)], \quad (2.4)$$

where $x = \bar{x}/a$, $r = \bar{r}/a$, $t = \bar{t}U_0/a$. Here, (U, V, P, H) represent the steady basic flow, which is non-dimensionalised following the boundary-layer scaling, for which $X = x/Re$ and $\bar{U} \sim Re \bar{V} \sim U_0$, and ϵ is a small parameter measuring the size of the unsteady perturbations around the mean flow, (u', v', p', h') .

2.1. The basic flow

The equations governing the basic flow are obtained by substituting the decomposition given by equations (2.1)-(2.4) into the incompressible, axisymmetric Navier-Stokes equations to yield, at $\mathcal{O}(\epsilon^0, Re^{-1})$, the steady axisymmetric boundary-layer equations,

$$U_X + \frac{1}{r}(rV)_r = 0, \quad (2.5)$$

$$U U_X + V U_r = We^{-1} H^{-2} H_X + \frac{1}{r}(rU_r)_r + G, \quad (2.6)$$

where $G = Re/Fr$ is a Stokes number, and subscripts denote partial derivatives. Notice that both the axial viscous stress and the radial pressure gradient have been neglected, since they are $\mathcal{O}(Re^{-2}) \ll 1$. Equations (2.5)-(2.6) are supplemented with the initial condition $X = 0 : U = u_0(r) = 2(1 - r^2)$, the boundary conditions $r = 0 : V = U_r = 0$ and $r = H : U_r = 0$, and the mass conservation constraint $\int_0^H U r dr = 1/2$. In the boundary condition at the free surface $r = H$, we have neglected terms $\mathcal{O}(Re^{-2}) \ll 1$ or smaller in the continuity of tangential stress at the interface. Moreover, we have also made the assumption that the external gas, of density ρ_g , has a negligible influence in the dynamics, which is a good approximation since the aerodynamic Weber number, $We_g = We \rho_g/\rho \ll 1$ (see Weber 1931; Gordillo & Pérez-Saborid 2005). In effect, note that $\rho_g/\rho \ll 1$, and the critical values of the Weber number $We_c \sim \mathcal{O}(1)$, as will be shown below. Finally, the axial pressure gradient $-P_X$ was obtained by the normal stress balance at the interface, where we have neglected both the axial curvature, with a relative error $\max[\mathcal{O}(Fr^{-2}), \mathcal{O}(Re^{-2})] \ll 1$, and the normal viscous stress at the interface, with an error $\mathcal{O}(Re^{-2}) \ll 1$. Thus, the pressure gradient is given by $-P_X = We^{-1} H^{-2} H_X$ with a small error $\max[\mathcal{O}(Fr^{-2}), \mathcal{O}(Re^{-2})] \ll 1$. An efficient and accurate method of lines was implemented to obtain the numerical solution of equations (2.5)-(2.6), as explained in detail by Gordillo *et al.* (2001). Typically, 200 lines were used in the computations.

The boundary layer equations (2.5)-(2.6), complemented with the boundary conditions discussed in the previous paragraph, have been studied in detail in the past. Numerical solutions in several representative cases were given by Duda & Vrentas (1967), while Oğuz (1998) provided a semi-analytical approach based on eigenfunction expansions. In addition, these studies showed good agreement between experiments and equations (2.5)-(2.6). The very near field of the jet, $X \rightarrow 0$, was considered by Goren (1966), who showed that the structure of the viscous layer which develops at the free surface resembles a Goldstein wake, while Tillet (1968) extended the analysis to include higher-order effects. On the other hand, the far field of the jet was considered by Goren & Wronski (1966), who provided with a complete description of the approach of the jet to the uniform

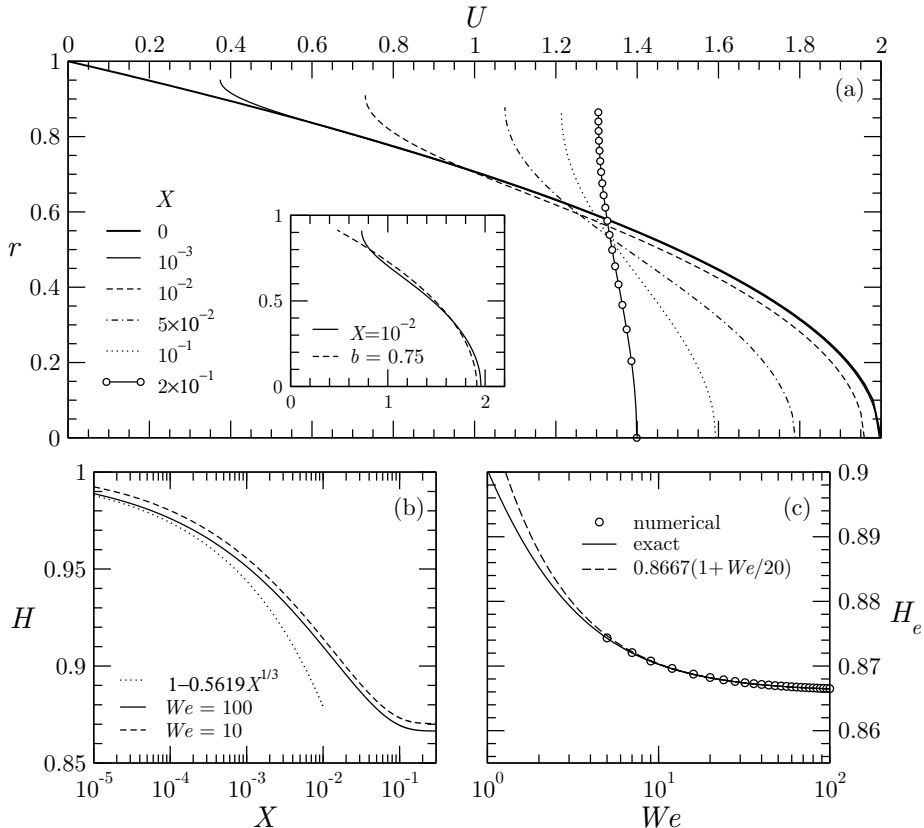


FIGURE 2. The basic flow for $G = 0$. (a) Velocity profiles for $We = 10$ at several downstream positions X , indicated in the legend. The inset shows a comparison of the velocity profile at $X = 0.01$, with a profile taken from the parametric family of Leib & Goldstein (1986*b*) for a value of the parameter $b = 0.75$. (b) Downstream evolution of the jet radius for $We = 10$ (solid line) and $We = 100$ (dashed line), together with the similarity solution due to Goren (1966) $H = 1 - 0.5619X^{1/3}$ (dotted line), and (c) asymptotic jet radius H_e as a function of We computed numerically (circles), compared with the exact solution (solid line) and its large Weber number approximation $\sqrt{3}/2(1 + We/20)$ (dashed line).

conditions achieved for $X \gg 1$. Finally, asymptotic solutions uniformly valid throughout the entire jet were given by Philippe & Dumargue (1991).

The main features of the basic flow considered here can be seen in figure 2, computed for the particular case of negligible gravitational effects, $G = 0$. Several examples of numerically computed velocity profiles along the relaxation region for $We = 10$ and different values of X are shown in figure 2(a). Notice that the initial region of jet acceleration is confined to a thin viscous layer adjacent to the free surface, as revealed by the velocity profile represented with a thin solid line for $X = 10^{-3}$. Mass conservation implies that the jet core must decelerate for larger values of X , as revealed by the velocity profile at $X = 10^{-2}$ shown as the thin dashed line in figure 2(a). The acceleration at the free surface, together with the deceleration at the axis, finally lead to an almost uniform velocity profile at $X = 0.2$, shown with circles in figure 2(a). A common feature of the local velocity profiles during relaxation is that they have an inflection point, whose radial position moves from the free surface towards the center of the jet as X increases. Note, however, that the velocity profiles proposed by Leib & Goldstein (1986*b*) to model the

relaxation region, namely $U_{\text{LG}} = (1 - br^2)/(1 - b/2)$ with $0 \leq b \leq 1$, are substantially different from the actual profiles in the relaxation region. This fact is illustrated by the inset of figure 2(a), which shows a comparison between the velocity profile obtained through equations (2.5)-(2.6) at $X = 0.01$ (solid line), and a profile taken from the family proposed by Leib & Goldstein (1986*b*), for a value of $b = 0.75$ (dashed line). Notice that, to perform the comparison, the parametric profile has been properly renormalised according to the expression $\tilde{U}_{\text{LG}}(r) = [1 - b(\tilde{r}/H)^2]/[H^2(1 - b/2)]$, with $0 \leq \tilde{r} \leq H$, such that $\int_0^H \tilde{r}U(\tilde{r})d\tilde{r} = 1/2$. The downstream evolution of the unperturbed jet radius, $H(X)$, is shown in 2(b) for two different values of the Weber number, namely $We = 10$ (solid line) and $We = 10$ (dashed line). Also shown in figure 2(b) is the similarity solution $H = 1 - 0.5619X^{1/3}$, obtained by Goren (1966) for $X \rightarrow 0$ and $We \rightarrow \infty$, which is seen to be in good agreement with the numerical solution for $We = 100$ and $X \lesssim 10^{-4}$. Another interesting feature of the jet, already pointed out by Oğuz (1998), is the fact that the radius relaxes sooner than the velocity profile. In effect, note from figure 2(b) that H takes its asymptotic value for $X \simeq 0.1$. In contrast, the dotted line represented in 2(b) reveals that the velocity profile is still far from uniform at this station, the velocities being $U(X = 0.1, r = 0) \simeq 1.6$ and $U(X = 0.1, r = H) \simeq 1.2$ at the centerline and the free surface, respectively. When surface tension effects are negligible, $We \gg 1$, it was shown by Harmon (1955) the jet velocity and radius reach limiting values $U_e = 4/3$ and $H_e = \sqrt{3}/2 \simeq 0.866$ at distances $X \sim \mathcal{O}(1)$ downstream, as can be shown by performing a global mass and momentum balance for the jet. More generally, multiplying equation (2.6) by r , integrating across the jet, and making use of equation (2.5), one obtains the following equation for the downstream evolution of the axial momentum of the jet, $J(X) = \int_0^H U^2 r dr$,

$$\frac{dJ}{dX} = \frac{1}{2We} \frac{dH}{dX} + G \frac{H^2}{2}, \quad (2.7)$$

which shows that, since $dH/dX < 0$, surface tension removes momentum from the jet, while gravity adds to it. In the particular limit $G \ll 1$, the last term of equation (2.7) is negligible in the region $0 \leq X \lesssim \mathcal{O}(1)$ where viscous relaxation takes place, and, integrating from $X = 0$ to $X = X_e \sim \mathcal{O}(1)$, where X_e is a station where the jet velocity profile is uniform, we obtain $U_e^2 H_e^2/2 - J_0 = (H_e - 1)/(2We)$. In addition, mass conservation implies that $U_e H_e^2 = 1$, and thus the relaxed jet radius for $G \ll 1$ is obtained from the cubic $H_e^3 + (2J_0 We - 1)H_e^2 - We = 0$, first obtained by Gavis (1964) for the particular case of a parabolic velocity profile at the jet exit, and whose solution has the expansion $H_e = (2J_0)^{-1/2} [1 + (1 - (2J_0)^{-1/2})/(4J_0 We) + \mathcal{O}(We^{-2})]$ for $We \gg 1$. The initial momentum flux, $J_0 = \int_0^1 U_0^2 r dr$, has the value $J_0 = 2/3$ for the parabolic profile and, in this case, $H_e = \sqrt{3}/2[1 + 3(2 - \sqrt{3})/(16We) + \mathcal{O}(We^{-2})] \approx \sqrt{3}/2(1 + 0.05/We)$, showing that the contribution of We rapidly becomes negligible as $We \gtrsim 1$. The function $H_e(We)$ is displayed in figure 2(c), where the numerically computed values of H_e , represented as open circles, are shown to be in very good agreement with the exact value, which solves the equation $H_e^3 + (4We/3 - 1)H_e^2 - We = 0$, and which is represented as a solid line in figure 2(c). Finally, the fact that the numerical results accomplish the global mass and momentum balance to a very high degree of accuracy, together with the good agreement found with Goren's similarity solution for $X \rightarrow 0$, serve as a stringent validation for the numerical code implemented here for the base flow.

2.2. The linear stability problem

The equations governing the linear dynamics of axisymmetric disturbances to the basic jet considered in §2.1 are obtained at $\mathcal{O}(\epsilon, Re^{-1})$ when (2.1)-(2.4) are substituted in the incompressible Navier-Stokes equations, leading to the following system of linearised stability equations,

$$u'_x + \frac{1}{r}(rv')_r = 0, \quad (2.8)$$

$$u'_t + U u'_x + U_r v' + p'_x - Re^{-1} \left[\frac{1}{r}(ru'_r)_r + u'_{xx} \right] = -Re^{-1} (U_X u' + V u'_r), \quad (2.9)$$

$$v'_t + U v'_x + p'_r - Re^{-1} \left[\left(\frac{1}{r}(rv')_r \right)_r + v'_{xx} \right] = -Re^{-1} (V_r v' + V v'_r), \quad (2.10)$$

to be solved with symmetry boundary conditions at the axis, $r = 0 : v' = u'_r = p'_r = 0$, as well as the following linearised boundary conditions at the free surface, $r = H(X)$:

$$v' - h'_t - U h'_x = Re^{-1} [H_X u' - V_r h'], \quad (2.11)$$

$$p' - 2 Re^{-1} v'_r + We^{-1} (H^{-2} h' + h'_{xx}) = - (WeRe)^{-1} H^{-1} H_X h'_x, \quad (2.12)$$

$$u'_r + v'_x + U_{rr} h' = 2 Re^{-1} [(u'_x - v'_r) H_X + (U_X - V_r) h'_x], \quad (2.13)$$

where equations (2.11)-(2.13) represent, respectively, the kinematic condition, the normal stress balance at the interface and the condition of zero shear stress at the interface. Notice that, as discussed in §2.1, the effect of the ambient gas has been neglected in equations (2.12) and (2.13). The terms appearing in the right hand sides of equations (2.8)-(2.13) represent non-parallel effects, and have been included since, as will be shown below, they have a crucial effect on the stability of the jet in the initial relaxation region.

Taking into account the fact that the most unstable perturbations to the basic jet have wavenumbers of the order of the jet radius, and thus evolve on the fast scale x , while the unperturbed jet evolves on the slow scale $X = x/Re$, a quasi-parallel approach will be used to solve the system of equations (2.8)-(2.13), whereby axisymmetric disturbances are represented as normal modes of the form

$$(u', v', p', h') = [\hat{u}(r), \hat{v}(r), \hat{p}(r), \hat{h}] e^{i(kx - \omega t)}, \quad (2.14)$$

where quantities with hats are the complex perturbation amplitudes, and the phase function incorporates the evolution of the local instability wave on the fast scale x . The substitution of equation (2.14) into the system (2.8)-(2.13) leads to the following system of linear equations for the normal modes,

$$ik\hat{u} + \frac{1}{r}(r\hat{v})_r = 0, \quad (2.15)$$

$$i(kU - \omega)\hat{u} + U_r \hat{v} + ik\hat{p} - Re^{-1} \left[\frac{1}{r}(r\hat{u}_r)_r - k^2\hat{u} \right] = -Re^{-1} (U_X \hat{u} + V \hat{u}_r), \quad (2.16)$$

$$i(kU - \omega)\hat{v} + \hat{p}_r - Re^{-1} \left[\left(\frac{1}{r}(r\hat{v})_r \right)_r - k^2\hat{v} \right] = -Re^{-1} (V_r \hat{v} + V \hat{v}_r), \quad (2.17)$$

which must be solved subjected to the symmetry conditions at the axis, $r = 0 : \hat{v} = \hat{u}_r = \hat{p}_r = 0$, as well as boundary conditions at $r = H(X)$ resulting from the transformation of equations (2.11)-(2.13) through equation (2.14),

$$\hat{v} - i(kU - \omega)\hat{h} = Re^{-1} (H_X \hat{u} - V_r \hat{h}), \quad (2.18)$$

$$\hat{p} - 2 Re^{-1} \hat{v}_r + We^{-1} (H^{-2} - k^2) \hat{h} = -(WeRe)^{-1} H^{-1} H_X ik\hat{h}, \quad (2.19)$$

$$\hat{u}_r + ik\hat{v} + U_{rr} \hat{h} = 2 Re^{-1} \left[(ik\hat{u} - \hat{v}_r) H_X + (U_X - V_r) ik\hat{h} \right]. \quad (2.20)$$

Since in this work we focus on the critical conditions for jet formability, we have solved the local eigenvalue problem, given by equations (2.15)-(2.20), with the aim at determining the convective or absolute nature of the local instability as a function of the downstream position X . The basic hypothesis underlying the present approach is that the *global* stability properties of the slender unperturbed jet obtained in §2.1 can be inferred from the *local* convective or absolute nature of the instability as a function of X . In this context, two different scenarios have been clearly identified in the particular case of weakly non-parallel flows (for a review, see Chomaz 2005): if the region of absolute instability (AI) starts right at the upstream boundary of the domain, the extent of the AI region must be larger than a certain minimum value for the global mode to be destabilised (Couairon & Chomaz 1999). In contrast, if the AI region is localised away from boundaries, a global mode is excited independently of its size (Pier *et al.* 1998). Although these findings have been rigorously demonstrated only for one-dimensional Ginzburg-Landau models, their application to actual fluid flows has been remarkably successful (see for instance Pier & Huerre 2001; Lesshafft *et al.* 2006).

Notice that, although the non-parallel terms in the right hand sides of equations (2.15)-(2.20) are usually disregarded when performing quasi-parallel stability analyses (however, see e.g. Gordillo & Pérez-Saborid 2005; Herrada *et al.* 2008), they are formally of the same order as the viscous terms, namely $\mathcal{O}(Re^{-1})$, and cannot be neglected except if $U_X \ll 1$ and $V \ll 1$. The latter conditions are not fulfilled in the initial relaxation region and, consequently, these non-parallel terms can be anticipated to play an important role in the local instability of the jet's near field. It is also important to emphasise that the quasi-parallel approach adopted in the present work is not completely rigorous, since base flow non-parallelism is accounted for only partially, through the right hand sides of equations (2.15)-(2.20). Alternative approaches to study the stability of the jet, like the parabolised stability equations (Herbert 1997), the linear global mode theory for weakly non-parallel flows (Chomaz *et al.* 1988; Huerre & Monkewitz 1990; Monkewitz *et al.* 1993; Le Dizès 1997), or a fully two-dimensional global stability analysis (Theofilis 2011), though more rigorous, are also substantially more involved than the quasi-parallel approach; they certainly constitute interesting topics for future work on the problem, but they are out of the scope of the present study.

The local stability problem given by the system of equations (2.15)-(2.20) was solved with a very efficient Chebyshev collocation method. For each value of X , the radial coordinate r was transformed into the basic interval $-1 \leq \xi \leq 1$ by means of the linear transformation $r = (1 - \xi)H(X)/2$. Introducing the vector of unknowns $\phi = (\hat{u}_i, \hat{v}_i, \hat{p}_i, \hat{h}, k\hat{u}_i, k\hat{v}_i, k\hat{h})^T$, $i = 1, \dots, N$, equations (2.15)-(2.20) can be written as a generalised eigenvalue problem of the form $A\phi = kB\phi$, where A and B are complex matrices of size $(5N+2) \times (5N+2)$. The derivatives are computed in physical space at the set of N Chebyshev collocation points, and the boundary conditions were implemented in the rows of the differentiation matrix corresponding to the points $r = 0$ and $r = H$. A value of $N = 30$ was enough to achieve very precise results.

3. Absolute instability in the jet: transition from jetting to dripping

This section is devoted to the presentation and analysis of the results obtained for the spatiotemporal stability of the jet.

3.1. Results for $G = 0$

Let us first consider the limit of negligible gravitational effects, $G \rightarrow 0$, in which case We and Re are the only parameters of the problem. Correspondingly, the critical Weber

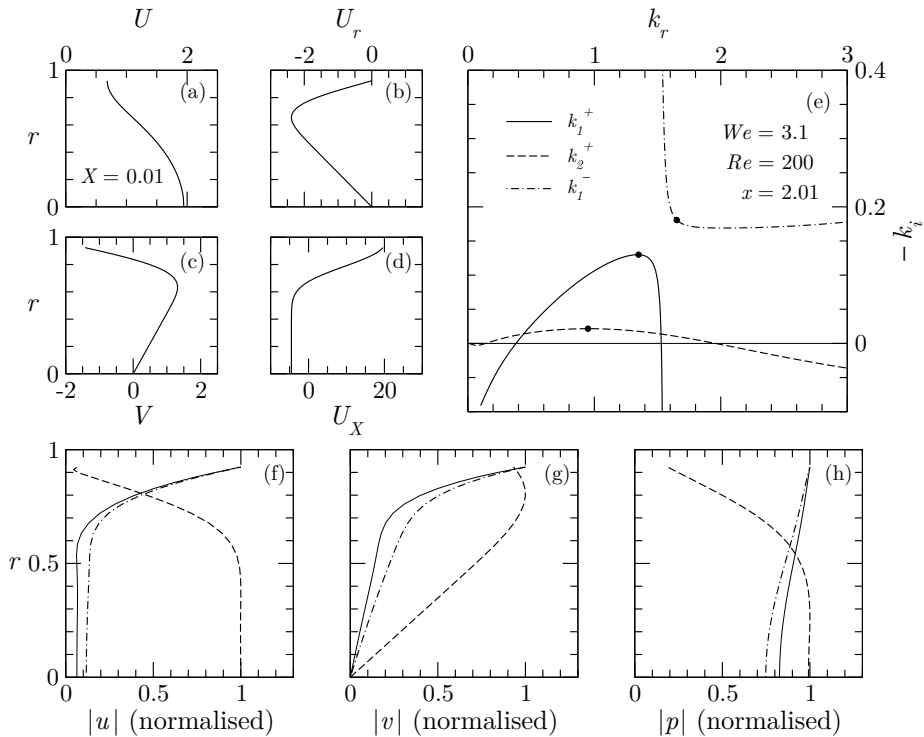


FIGURE 3. Radial profiles of (a) U , (b) U_r , (c) V and (d) U_X , for $We = 3.1$ and $X = 0.01$. (e) Corresponding spatial stability branches for $Re = 200$. Normalised moduli of the eigenfunctions corresponding to the eigenvalues of the three spatial modes shown as solid circles in panel (e): (f) axial velocity, $|u|$, (g) radial velocity, $|v|$ and (h) pressure, $|p|$.

number for the onset of absolute instability is a function $We_c(Re)$, which was obtained by Leib & Goldstein (1986a) in the particular case of a jet of constant radius and uniform velocity profile. Figure 3 summarises the results obtained for a jet with $We = 3.1$ at the particular downstream position $X = 0.01$. Panels 3(a)-3(d) show the corresponding base flow profiles of U, U_r, V and U_X , respectively, which appear as coefficients in the stability equations (2.15)-(2.20) and in their boundary conditions. Note, in particular, that the non-parallel convective terms $Re^{-1}(U_X \hat{u} + V \hat{u}_r)$ and $Re^{-1}(V_r \hat{v} + V \hat{v}_r)$ respectively appearing in equations (2.16) and (2.17) will be important for $X \ll 1$ and moderately large values of Re . Figure 3(e) shows three spatial stability branches corresponding to this particular basic flow for $Re = 200$: two of them, denoted by k_1^+ (solid line) and k_2^+ (dashed line), contribute to the downstream response of the jet to forcing, while the k_1^- branch (dash-dotted line) contributes to the upstream response. It must be emphasised that many other *stable* spatial branches were found, but only these three are relevant to the present work. The fact that the two branches k_1^+ and k_2^+ contribute to the downstream response can be deduced from their movement in the k -plane when ω_i is varied: for values of ω_i larger than the maximum temporal growth rate for the parameter combination corresponding to figure 3, these two branches belong to the $k_i > 0$ half-plane, whereas the branch k_1^- remains in the opposite one, with $k_i < 0$. Notice also from figure 3(e) that both downstream branches have unstable frequency ranges in which $k_i < 0$, corresponding to linear waves with exponentially increasing amplitudes downstream from their source. On the contrary, branch k_1^- is stable, leading to exponentially decreasing amplitudes upstream from the source. To provide a more

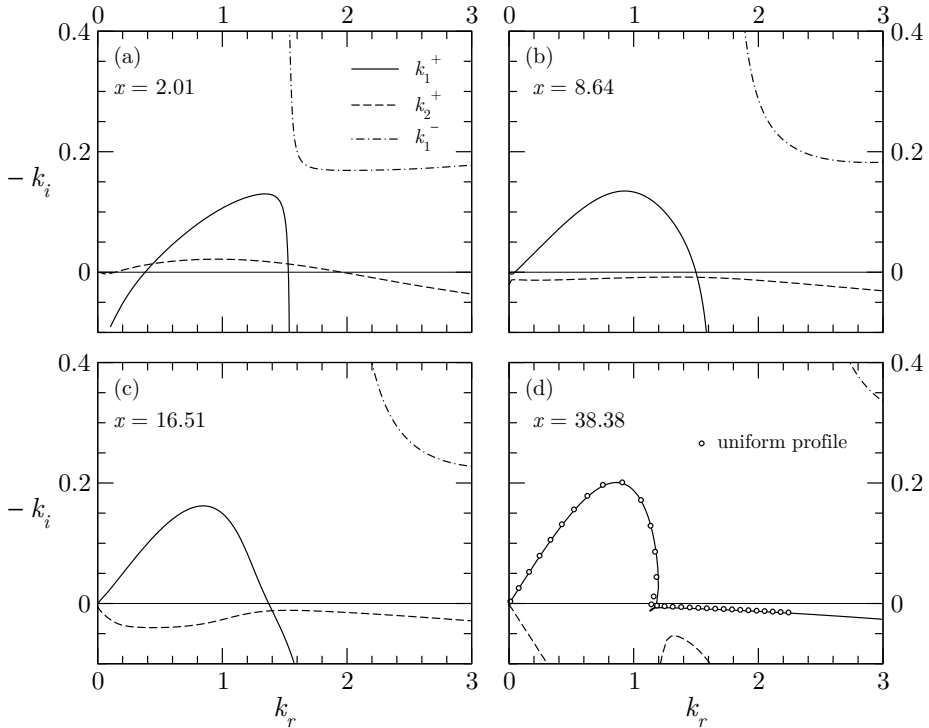


FIGURE 4. Evolution of the spatial branches for $Re = 200$, $We = 3.1$, and different downstream positions along the jet: (a) $x = 2.01$, (b) $x = 8.64$, (c) $x = 16.51$ and (d) $x = 38.38$. The hollow circles in panel (d) correspond to the unstable branch of the Rayleigh-Chandrasekhar dispersion relation for a jet with uniform velocity profile.

complete picture of these spatial instability modes, figures 3(f)-(h) respectively show the normalised moduli of the eigenfunctions of axial velocity, $|u|$, radial velocity, $|v|$ and pressure, $|p|$, for the eigenvalues marked with a solid circle on top of the corresponding spatial branch in figure 3(e). Figures 3(f)-(h) reveal that the eigenfunctions of the spatial modes k_1^+ (solid lines) and k_1^- (dash-dotted lines), reach their maxima at the interface, $r = H$, and in fact resemble the Rayleigh modes appearing in unstretched jets with uniform velocity profiles. It is also interesting to note that non-parallel effects break the translation invariance, introducing a low wavenumber cut-off to the unstable k_1^+ branch, such that $\omega_i < 0$ for $k_r = 0$. On the other hand, the eigenfunctions associated to the unstable downstream branch k_2^+ , shown as dashed lines in figures 3(f)-(h), indicate that this mode is of a different nature, its maximum amplitude taking place inside the jet. A parametric study, not shown here for brevity of presentation, reveals that the k_2^+ mode is unstable only for large enough values of both Re and We , and small enough values of X . Thus, it is a *surface wave mode*, which arises due to the interaction of shear and interface deflection (see Miles 1960; Smith & Davis 1982, for a detailed account).

The spatial instability modes evolve continuously along the jet. Thus, for instance, figure 4 shows the spatial branches for $We = 3.1$ and $Re = 200$, performed at four different values of x , namely (a) $x = 2.01$, (b) $x = 8.64$, (c) $x = 16.51$ and (d) $x = 38.38$, with panel (a) being identical to figure 3(e). Notice that the k_1^+ mode evolves downstream to eventually become the standard unstable branch of the Rayleigh-Chandrasekhar viscous dispersion relation in the developed region of the jet, i.e. for

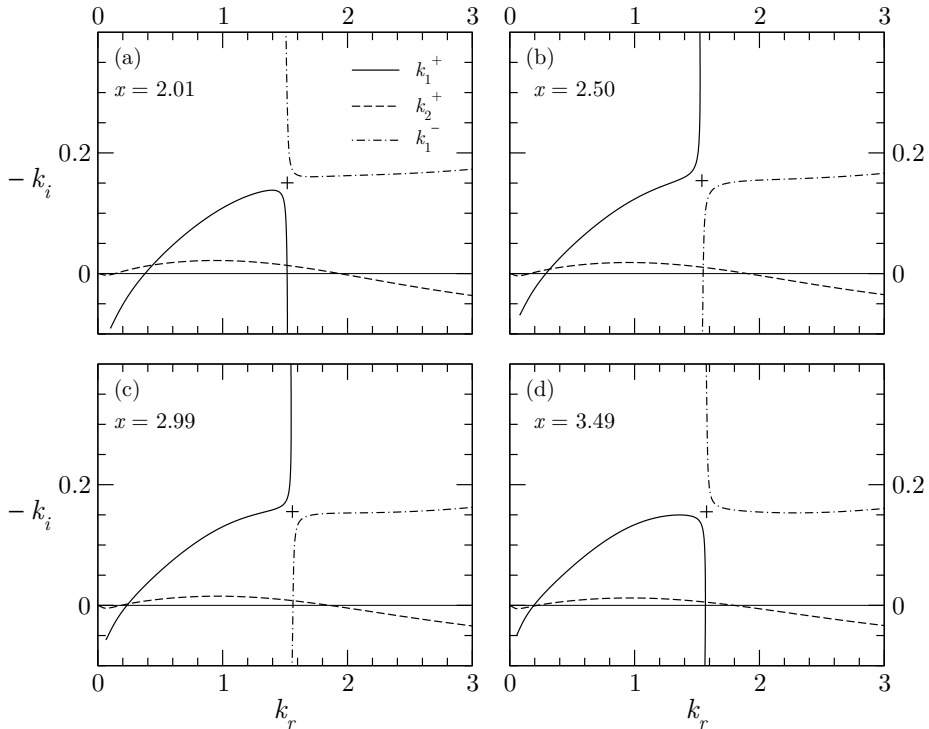


FIGURE 5. Downstream evolution of the spatial branches for $Re = 200$, $We = 3$ and different downstream positions along the jet: (a) $x = 2.01$, (b) $x = 2.50$, (c) $x = 2.99$ and (d) $x = 3.49$. The cross marks the position of the double root, computed with the method of Deissler (1987).

$X \gtrsim \mathcal{O}(10^{-1})$. In effect, the hollow circles in figure 4(d), computed with the viscous dispersion relation for a jet with uniform velocity profile, are seen to lie on top of the k_1^+ mode at the station $x = 38.38$. Please also note that the wavenumber k has been made dimensionless with the injector radius, a , instead of the local radius of the jet $aH(X) < a$, which explains the shift towards higher k observed in figure 4(d) in both the maximum and cut-off wavenumbers, with respect to their canonical counterparts. In contrast with the k_1^+ mode, the k_2^+ branch becomes stable sufficiently far downstream along the relaxation region, as expected from the fact that the base flow shear decreases as x increases. Note that for the particular parameter values $We = 3.1$, $Re = 200$ the k_2^+ mode is already stable at $x = 8.64$, as can be seen in figure 4(b). In fact, irrespective of the values of Re and We , this mode always stabilises at sufficiently large values of x for which the base flow shear becomes small enough. Finally, it is important to point out that the instability is of convective type everywhere along the jet for $We = 3.1$ and $Re = 200$, since no pinching between downstream (k^+) and upstream (k^-) branches takes place at any value of x . Consequently, the signaling problem is well posed in this case, and the k_1^+ branch could then be used to describe the exponential downstream amplification of small disturbances leading to the breakup of the jet at some distance from the outlet.

Figure 5 displays the results of a spatial analysis performed for the same value of $Re = 200$, but a slightly smaller value of $We = 3$, for which a different scenario emerges. Thus, figure 5(a) shows that, at $x = 2$, the k_2^+ branch remains practically unchanged with respect to the case with $We = 3.1$, the k_1^+ branch gives rise to a convective

instability within a certain range of frequencies, and the k_1^- branch has approached the k_1^+ branch. This behaviour persists along the jet down to the station $x_{ca} \simeq 2.11$, where the k_1^+ and k_1^- solutions touch at a double root, ($k_0 \simeq 1.525 - 0.151i, \omega_0 \simeq 0.682 + 0i$), of the dispersion relation, indicating the switch from a locally convective to a locally absolute instability in the jet at this particular position. Figures 5(b) and 5(c) show the structure of the k -plane at $x = 2.5$ and $x = 2.99$, downstream of the critical station where the mode interaction takes place. Note that k_1^+ and k_1^- branches have exchanged identities as a consequence of their interaction in the neighborhood of the double root. More precisely, the spatial stability analysis becomes ill defined in this region since the different spatial branches can no longer be attributed to the downstream or upstream response of the flow. Instead, the local instability is absolute in this region due to the direct resonance between the k_1^+ and k_1^- modes, giving rise to exponential amplification of perturbations both upstream and downstream from their source (for a detailed discussion, see Huerre & Monkewitz 1990; Chomaz 2005). For the combination of parameters of figure 5, the local absolute instability persists down to the station $x_{ac} \simeq 3.28$, where it becomes convective again, and so it remains for $x > x_{ac}$. An example is shown in figure 5(d), calculated for $x = 3.49$, where it can be seen that the k_1^+ and k_1^- branches have interacted again at a double root, and recover the physical meaning they had in the region $x < x_{ca}$. A similar study of the k -plane was performed for the same value of the Reynolds number, $Re = 200$, and different values of We , showing a similar sequence of events whenever $We \lesssim 3.07$. However, for $We \gtrsim 3.07$ the analysis revealed that the double root did not take place anywhere along the jet, indicating that the instability is convective everywhere in this case. Since, in the absence of feedback, the appearance of an unstable global mode requires the existence of a region of local absolute instability, this means that the jet with $Re = 200$ should be globally stable for $We \gtrsim 3.07$.

In order to extend the analysis to other values of Re , while avoiding the need for a complete characterization of the complex k -plane, we implemented the method developed by Deissler (1987) for the direct computation of double roots, (k_0, ω_0) , of the dispersion relation. In particular, the crosses plotted in figure 5 were computed following this method. Once the double root was converged for fixed values of (Re, We, x) , it was followed in parameter space by means of a standard continuation method. Several examples of these computations can be seen in figure 6, which shows the downstream evolution of the *absolute growth rate*, $\omega_{0,i}(x)$, for several values of the Reynolds and Weber numbers, as indicated in the panels. The dots in figure 6(c) correspond to the four downstream positions analysed in figure 5. Figure 6 shows that the local instability is convective near the outlet, $\omega_{0,i}(x = 0) < 0$, independently of the values of Re and We . Therefore, the critical station x_{ca} at which the instability type changes from convective to absolute, $\omega_{0,i}(x_{ca}) = 0$ with $d\omega_{0,i}/dx > 0$, always takes place downstream of the outlet, $x_{ca} > 0$. Moreover, figure 6 reveals that, for a fixed value of Re , the absolute growth rate $\omega_{0,i}$ decreases as We increases, as expected from physical grounds. For instance, figure 6(a) shows that, for $Re = 10$ and $We = 1.05$ (solid line), a region of absolute instability, $\omega_{0,i} > 0$, exists within the jet. However, for a slightly larger value of $We = 1.1$ (dashed line), the jet is locally convectively unstable throughout the domain, $\omega_{0,i}(x) < 0 \forall x$. Consequently, if the critical Weber number, We_c , is defined according to the condition $\max[\omega_{0,i}(x; We_c, Re)] = 0$, it is such that $1.05 \leq We_c \leq 1.1$ for $Re = 10$. A similar trend can be seen to hold for the other Reynolds numbers shown in figure 6, with the corresponding values of We_c increasing with Re . Thus, from figures 6(b)-6(d) it is deduced that $1.7 \leq We_c(Re = 50) \leq 1.75$, $3 \leq We_c(Re = 200) \leq 3.1$, and $9 \leq We_c(Re = 1000) \leq 9.5$, respectively. To obtain more precise values of the

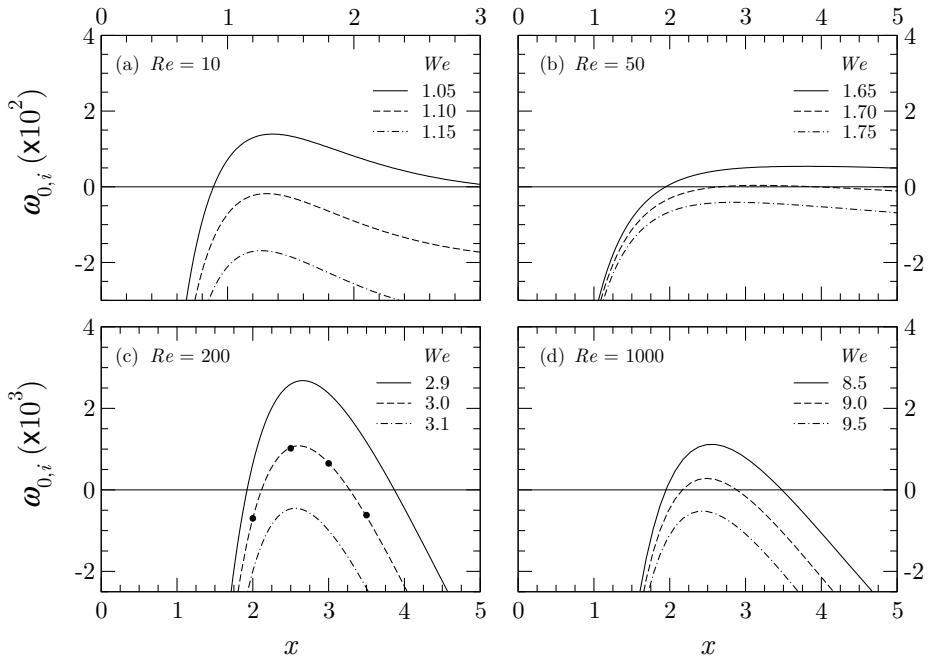


FIGURE 6. Downstream evolution of the absolute growth rate, $\omega_{0,i}(x)$, for $Re = (10, 50, 200, 1000)$ in panels (a)-(d), respectively, and several values of We indicated in the legends. The dots in panel (c) indicate the positions corresponding to figure 5.

function $We_c(Re)$, the curves were computed for small increments of Re in the range $10 \leq Re \leq 1000$, and the corresponding values of We_c were then obtained by a standard root finding technique together with a continuation method.

Figure 7 summarises the results obtained in the present section for the case without gravity, $G = 0$. Thus, the dependence of the critical Weber number on the Reynolds number is shown in figure 7(a), both for a jet with uniform velocity profile, obtained by Leib & Goldstein (1986a) (dashed line), and for a jet with fully-developed profile at the outlet considered in the present work (solid line). Both results are seen to coincide at the point $(Re, We) \simeq (145, 2.6)$. On the one hand, for $Re < 145$, the jet with parabolic outlet profile is slightly more stable than the uniform profile jet, in the sense that the former has smaller associated values of We_c than the latter. On the other hand, for $Re > 145$, while the uniform profile jet tends monotonically to the inviscid asymptote $We_c \rightarrow 3.1$ as $Re \rightarrow \infty$ (Leib & Goldstein 1986b), the slope of the curve $We_c(Re)$ is seen to increase with Re . Note that, as mentioned in §1, an upper limit of $Re = 1000$ has been set in the computations in order to ensure laminar flow in the jet. Nevertheless, notice that both results differ substantially in the range $200 \lesssim Re \lesssim 1000$, with the parabolic jet reaching values as high as $We \simeq 9.25$ at $Re = 1000$. Unfortunately, although several authors have reported experimental results of the jetting/dripping transition under microgravity or reduced gravity conditions using nozzles (see for instance Vihinen *et al.* 1997; O’Donnell *et al.* 2001; Osborne & Steinberg 2006), to the best of the author’s knowledge no data is available in the literature for low Ohnesorge number capillary jets discharging from long needles in this case. Consequently, new experiments would be needed in order to check the results of figure 7. It is important to emphasise the strong differences between our results and those obtained by Leib & Goldstein (1986b) in their inviscid spatiotemporal

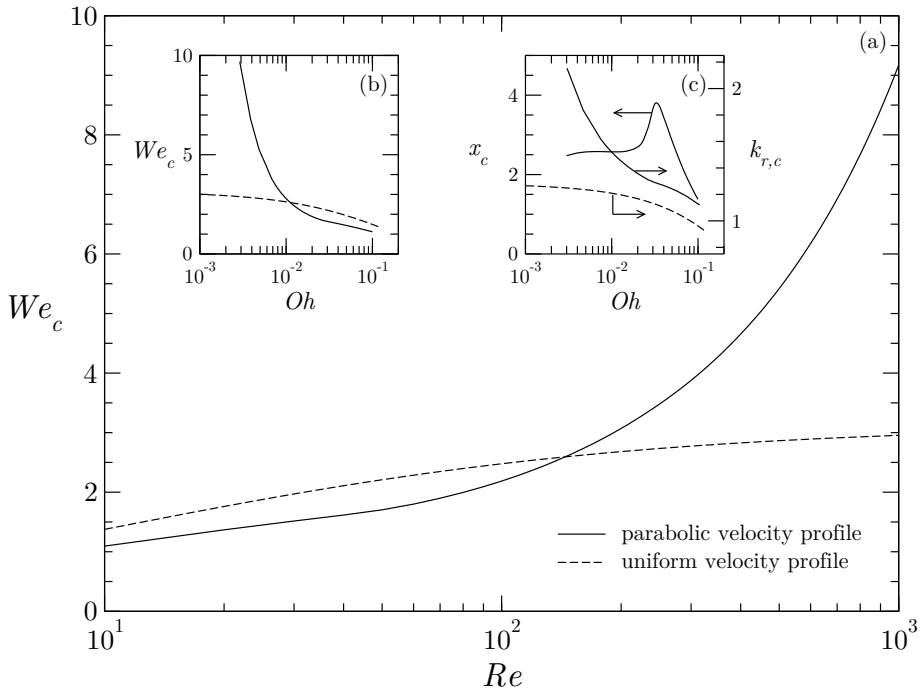


FIGURE 7. (a) Critical Weber number, We_c , as a function of Re for the onset of absolute instability without gravity, $G = 0$. (b) The function $We_c(Oh)$ and (c) the functions $x_c(Oh)$ (left axis) and $k_{r,c}(Oh)$ (right axis). The solid line shows the results obtained for parabolic velocity profile at the outlet, while the dashed line corresponds to uniform velocity profiles (Leib & Goldstein 1986a).

analysis of the parametric family of profiles $(1 - br^2)/(1 - b/2)$, $0 \leq b \leq 1$, aimed at modeling the effects of viscous relaxation. In particular, figure 9 of Leib & Goldstein (1986b), which shows We_c as a function of the parameter b , gives a range of values for the critical Weber number going from $We_c \simeq 0.45$ for $b = 1$, corresponding to the parabolic Poiseuille profile, to $We_c \simeq 3.1$ for $b = 0$, i.e. the inviscid asymptote for the uniform profile, having a local maximum $We_c \simeq 3.24$ at $b \simeq 0.14$. Although Leib & Goldstein (1986b) argue that the effect of the downstream evolution of the jet would correspond to a parametric movement from $b = 1$ to $b = 0$, it is clear that the value of $We_c < 3.25$ independently of the relationship between the parameter b and the downstream position x , leading to results completely different from those shown in figure 7(a). Since the values of Re and We are linked through the Ohnesorge number by $Oh = We^{1/2}/Re$, the critical conditions can alternatively be described, without loss of generality, by the function $We_c(Oh)$ represented in figure 7(b), whose usefulness lies in the fact that Oh is independent of the jet velocity. In addition, we have also plotted in figure 7(c) the dependence of the real part of the absolute wavenumber evaluated at the critical conditions ($k_{r,c}$, right axis), as well as the station x_c where marginal local absolute instability takes place (left axis). Figure 7(c) reveals, in particular, that the absolute mode associated to the uniform profile jet (dashed line) has a longer wavelength compared to that of a jet with parabolic outlet profile (solid line). Moreover, in the latter case the marginal station is seen to present a non-monotonic behaviour, varying in the range $1.5 \lesssim x_c \lesssim 4$, with a low- Oh plateau at $x_c \simeq 2.5$.

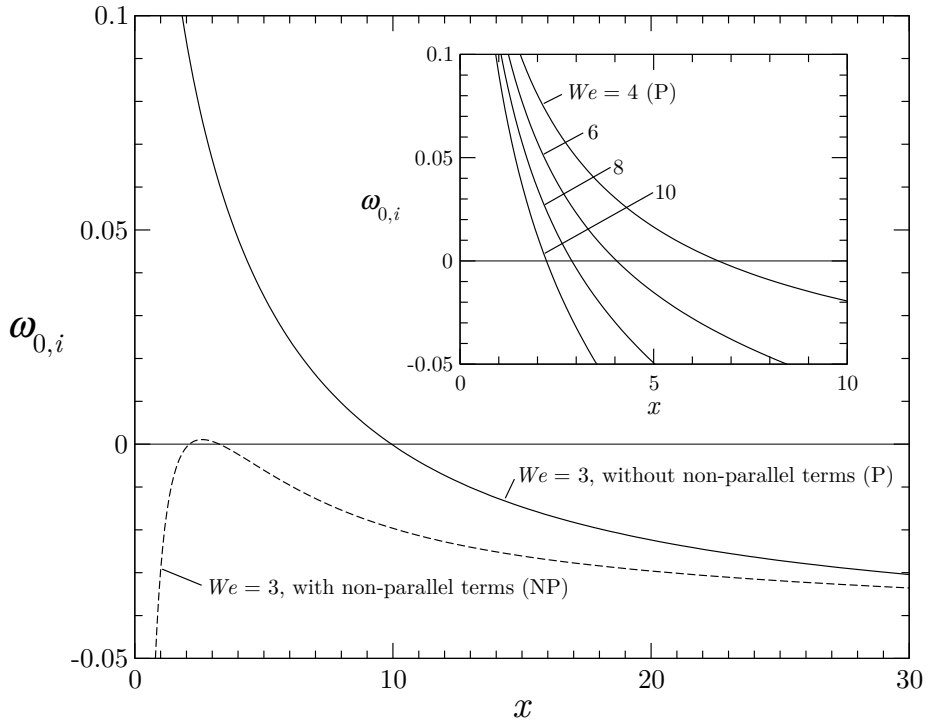


FIGURE 8. Downstream evolution of $\omega_{0,i}$ for $Re = 200$ and $We = 3$, computed with (case NP, dashed line) and without (case P, solid line) non-parallel terms in the stability equations. The inset shows the function $\omega_{0,i}(x)$, calculated for the case P, for $Re = 200$ and values of $We = (4, 6, 8, 10)$, which predicts a region of absolute instability close to the nozzle regardless of the value of We .

The picture described above changes completely when non-parallel terms are disregarded in the stability equations, i.e. when the right hand sides of equations (2.16)-(2.20) are neglected. This approximation will hereafter be referred to as *case P*, in contrast with the computations performed retaining the non-parallel terms, which will be called *case NP*. Figure 8 shows the function $\omega_{0,i}(x)$ for $Re = 200$ and $We = 3$, calculated both for the P and NP cases (solid and dashed lines, respectively). Figure 8 reveals that both approaches give markedly different results for values of $x \lesssim 20$, i.e. values of $X \lesssim \mathcal{O}(0.1)$, for which non-parallel terms give order unity contributions to the stability properties at moderately large values of Re , as was previously noted. In particular, the values of $\omega_{0,i}$ in case P are larger than in case NP all along the jet. Since far downstream the jet velocity profile tends to be uniform, and its radius tends to a constant value, both results tend to a common limit as $x \rightarrow \infty$. However, the crucial difference lies in their behaviour near the outlet. As can be observed in figure 8, in case P the value of $\omega_{0,i}$ increases monotonically as $x \rightarrow 0$. In effect, the value of the absolute growth rate at a given jet station results from a competition between the degree of instability and the convective velocity of the growing disturbances. Since the eigenfunctions of the k_1^+ and k_1^- modes peak at the interface [see figure 3], it is expected that the decrease in surface velocity which takes place as $x \rightarrow 0$ leads to an increase in the values of $\omega_{0,i}$. Although the same reasoning applies to the NP model, in this case non-parallel terms introduce a *stabilising* influence which compensates the destabilisation associated with the reduced free-surface velocity. For instance, note that the non-parallel convective term in the x -momentum equation (2.16), $U_X \hat{u}$, enhances the downstream transport of the perturbations, thus

leading to the reduced values of $\omega_{0,i}$ observed in figure 8 for case NP, when compared to case P. Moreover, this stabilising effect is enhanced as x decreases, as a consequence of the fact that the acceleration of the base flow at the interface, $U_X(X, r = H)$, increases very fast as $X \rightarrow 0$. In particular, as mentioned before, $\omega_{0,i} < 0$ at the outlet, and the locally absolutely unstable region always takes place inside the jet in case NP. In addition, the inset of figure 8 shows that, although in case P the size of the absolutely unstable region decreases as We increases, it does always exist sufficiently close to the exit and, in particular, $\omega_{0,i} > 0$ at $x = 0$ irrespective of the value of We . It is worth mentioning that a behaviour similar to the case P was found in the case of planar liquid sheets undergoing viscous relaxation by Söderberg (2003), where non-parallel terms were discarded in the stability equations, and a region of absolute instability was shown to be present close to the nozzle. As happens here, although the size of the absolutely unstable region decreases as We increases, it does not lead to a clear identification of a globally stable jet. Moreover, this behaviour poses a fundamental problem when considering the spatial instability of the jet, not specifically addressed here, which would always be ill-defined due to the presence of the absolutely unstable region near the outlet. In the remainder of the paper, the analysis will be performed retaining the non-parallel terms in the linear stability equations.

3.2. Results for finite G : jetting/dripping transition in water jets

Let us now present several results obtained taking gravity into account. As pointed out by Le Dizès (1997), the parameters of the problem, We, Re and G , are not independent from each other given the values of the liquid properties ρ, ν and σ , and the gravitational acceleration g . In looking for an alternative set of parameters that enables a more straightforward comparison with experimental results, it is convenient to express the dependence on the length scale through the Bond number, $Bo = \rho g a^2 / \sigma$. The values of the Stokes and Reynolds numbers, needed in the computation of the basic flow and its stability, are then uniquely specified in terms of the Weber number as $G = (Bo^5 / Mo)^{1/4} We^{-1/2}$ and $Re = (Bo / Mo)^{1/4} We^{1/2}$, where $Mo = \nu^4 \rho^3 g / \sigma^3$ is the Morton number of the liquid, independent of a and Q . As a result, the critical Weber number for the appearance of absolute instability in the jet can be expressed alternatively as a function of the form $We_c(Bo, Mo)$, which for a given liquid simplifies to $We_c(Bo)$. The results presented in this section have been computed for water at room temperature, for which $Mo \simeq 2.52 \times 10^{-11}$, corresponding to the experiments performed by Clanet & Lasheras (1999). Notice that, in the particular case of water, the Stokes number is $G \simeq 446 Bo^{5/4} We^{-1/2}$ and, since it will be seen that $We_c \lesssim \mathcal{O}(1)$, the effect of gravity cannot be neglected except for sufficiently small injector diameters, $Bo \lesssim \mathcal{O}(10^{-2})$ (see figure 10).

The spatiotemporal analysis presented in this section follows the same lines as that of §3.1. It is important to emphasise that, although the local stability properties obtained for the jet with $G > 0$ present quantitative differences from those presented in §3.1 for the case $G = 0$, the phenomenology is qualitatively similar. In particular, the spatiotemporal stability properties are governed by the interaction of the same spatial instability modes described in §3.1, namely k_1^+ and k_1^- . Consequently, in this section we will directly present computations of the double root (k_0, ω_0) . Specifically, for given values of Bo and We , (k_0, ω_0) was computed as a function of x by means of a continuation method, with the values of G and Re obtained as described in the previous paragraph, with the aim at obtaining the function $We_c(Bo)$ for water jets. The results obtained are summarised

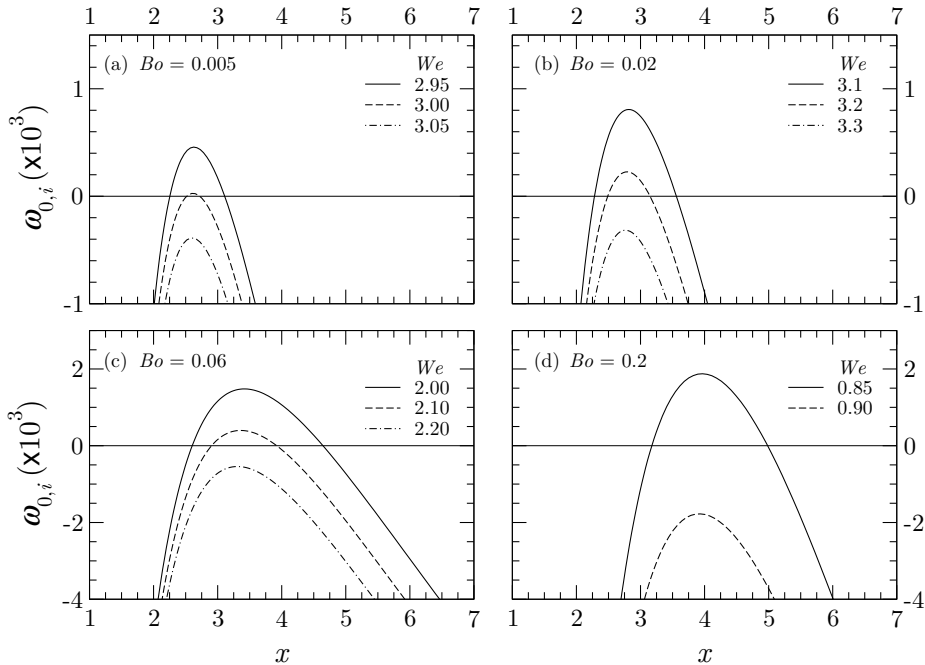


FIGURE 9. Downstream evolution of the absolute growth rate, $\omega_{0,i}(x)$, for $Mo = 2.52 \times 10^{-11}$, corresponding to water at room temperature, and (a) $Bo = 0.005$, (b) $Bo = 0.02$, (c) $Bo = 0.06$ and (d) $Bo = 0.2$, and different values of We indicated in the legends.

in figures 9 and 10.

The downstream evolution of the absolute growth rate, $\omega_{0,i}(x)$, is represented in figures 9(a)-9(d) for the values of $Bo = (0.005, 0.02, 0.06, 0.2)$, respectively, and several values of We as indicated in the legends. Note that the shapes of the curves are similar to those shown in figure 6: the maximum value $\omega_{0,i}^m$ takes place inside the jet at a station x_m which varies from $x_m \simeq 2.5$ for $Bo = 0.005$, to $x_m \simeq 4$ for $Bo = 0.2$. Moreover, for each value of Bo , $\omega_{0,i}^m$ decreases as We increases. Thus, for instance, figure 9(a) shows that, for $Bo = 0.005$ and $We = 2.95$ (solid line), $\omega_{0,i} > 0$ in the range $2.25 \lesssim x \lesssim 3.12$. However, for $We = 3$ (dashed line), the flow is only marginally absolutely unstable near $x \simeq 2.3$, and it is locally convectively unstable throughout for slightly larger value of $We = 3.05$ (dash-dotted line). Consequently, the critical Weber number accomplishes $3 < We_c < 3.05$ for $Bo = 0.005$. A similar trend is observed in figures 9(b)-9(d), with the value of We_c showing a non-monotonic behaviour for increasing values of Bo . In effect, note that $3.2 < We_c(Bo = 0.02) < 3.3$, $2.1 < We_c(Bo = 0.06) < 2.2$ and $0.85 < We_c(Bo = 0.2) < 0.9$.

Following a procedure similar to that described in §3.1 for the case without gravity, a more detailed calculation was performed to obtain an accurate representation of the function $We_c(Bo)$ in the range $0.001 \leq Bo \leq 0.2$. The upper limit in Bo was set in the computations due to the fact that the slenderness requirement $1 \ll Fr = We/Bo$ is manifestly violated for $Bo \gtrsim 0.2$. On the other hand, since $Re = (Bo/Mo)^{1/4} We^{1/2}$, $We_c^{1/2} \gtrsim \mathcal{O}(1)$ and $Bo \gg Mo$, the restriction $Re \gg 1$ is always accomplished in this case. Figure 10 shows the function $We_c(Bo)$ obtained in the present work for the cases without gravity (dash-dotted line), and with gravity (solid line). Please note that the

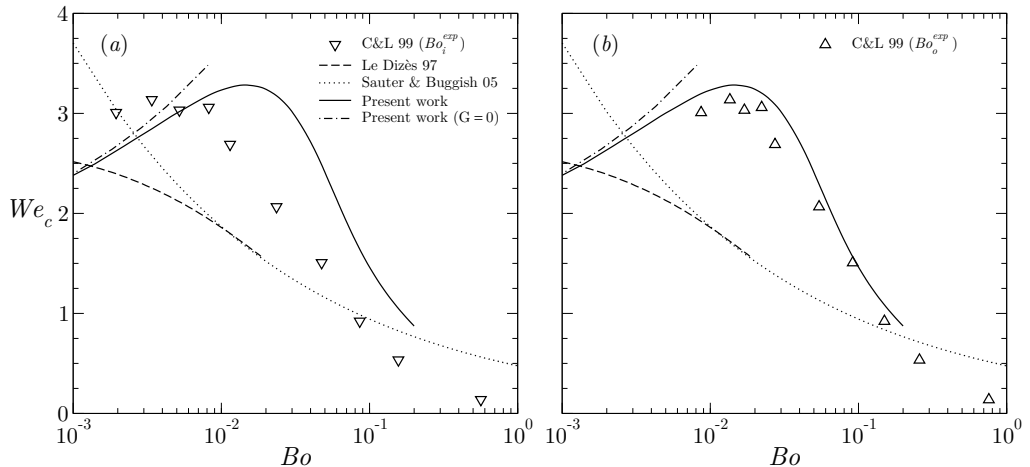


FIGURE 10. The function $We_c(Bo)$ for transition from jetting to dripping in water obtained from the experiments of Clanet & Lasheras (1999), using (a) the inner needle radius (∇), and (b) the outer needle radius (Δ), to compute the value of Bo . Also shown are the results of the present work with and without gravity (solid and dash-dotted lines, respectively), as well as those by Le Dizès (1997) (dashed line) and Sauter & Buggisch (2005) (dotted line).

dash-dotted line in figure 10 corresponds to the function $We_c(Re)$ obtained in §3.1, with the Reynolds number given by $Re = (Bo/Mo)^{1/4} We^{1/2}$, as explained above. The results were computed for a value of $Mo = 2.52 \times 10^{-11}$, corresponding to water at room temperature. Also shown are the experimental results of Clanet & Lasheras (1999) for the transition from jetting to dripping in water jets discharging from needles long enough for the velocity profile to be fully developed at the outlet (∇, Δ). As mentioned in §2, these experiments were conducted with hypodermic needles having a finite wall thickness, and the contact line was always pinned at the *outer* edge of the exit section. Therefore, an unambiguous comparison between theory and experiments is precluded by the fact that the flow configuration is not exactly the same as that considered in the present work, which only considers the case of a vanishingly thin wall thickness. In particular, to compute the values of the Weber and Bond numbers associated to the experimental data points obtained by Clanet & Lasheras (1999), one may arbitrarily choose either the inner or the outer radius as characteristic length scale. Note that Sauter & Buggisch (2005), who also disregarded finite wall thickness effects in their analysis, faced the same problem when comparing their results with those by Clanet & Lasheras (1999). In particular, Sauter & Buggisch (2005) chose the inner diameter of the nozzle to obtain the experimental values of both We and Bo . Here, we shall also choose the inner radius to compute the experimental value of the Weber number, $We^{\text{exp}} = \rho Q_{\text{exp}}^2 / (\pi^2 \sigma a_i^3)$, where Q_{exp} is the experimental volume flow rate and a_i is the inner needle radius. Regarding the Bond number, we decided to include two different data series, where Bo is based either on the inner or on the outer radius. Thus, figures 10(a) and 10(b) respectively make use of the expressions $Bo_i^{\text{exp}} = \rho g a_i^2 / \sigma$ and $Bo_o^{\text{exp}} = \rho g a_o^2 / \sigma$ for the Bond number, where a_o represents the outer radius. In addition, figure 10 also includes the results obtained by Le Dizès (1997) and Sauter & Buggisch (2005), hereafter referred to as LD97 and S&B05, for liquid jets with uniform velocity profiles (dashed and dotted lines, respectively). The results of LD97 and S&B05 coincide in the range $0.009 \lesssim Bo \lesssim 0.02$, but separate from each other for $Bo \lesssim 0.009$, the values of We_c given by S&B05 being larger than those of LD97 in that range. Nevertheless, both curves are seen to

underestimate the experimental values of We_c up to $Bo \simeq 0.1$, where the result of S&B05 crosses the experimental data, overestimating them for $Bo \gtrsim 0.1$. In contrast, the results obtained in §3.2 of the present work (solid line) are seen to provide better overall agreement with the experimental trend in a wide range of Bond numbers, especially in the case of figure 10(b), where the outer radius is used to compute the Bond number. The result obtained in §3.1 for the buoyancy-free jet, $G = 0$, (dash-dotted line) agrees with the full computation only for values of $Bo \lesssim 0.005$. Thus, in addition to viscous relaxation, the effect of gravity must also be taken into account in the stability analysis to properly describe the transition from jetting to dripping observed in experiments.

4. Conclusions

A spatiotemporal linear stability analysis has been performed with the aim of predicting the appearance of local absolute instability in capillary jets undergoing velocity profile relaxation at large Reynolds and Froude numbers. Although the reference case of a fully developed flow at the exit was analysed in detail, the approach presented in this work could also be used to study other exit velocity profiles, e.g. those corresponding to nozzles or short injection tubes. Nevertheless, it could well be that several conclusions drawn from the present work apply also to other configurations, independently of the exact shape of the initial velocity profile. Thus, for instance, we have highlighted the importance of retaining non-parallel terms in the local stability equations, by comparing computations performed with and without these terms. It is important to emphasise that non-parallel terms enter the local stability problem at the same order as viscous effects in the perturbations, namely Re^{-1} . Consequently, they can be neglected only when base flow variations and transverse velocities become small, as happens sufficiently far downstream from the outlet, where the computations performed with and without non-parallel terms coincide. However, it is precisely the region near the outlet where absolute growth rates become larger due to the small values of the free surface velocity. In fact, when calculated without non-parallel terms, the slope of the local absolute growth rate satisfies $d\omega_{0,i}(x)/dx < 0$ as $x \rightarrow 0$. This behaviour is similar to that found by Söderberg (2003) in his analysis of the relaxing two-dimensional liquid sheet for values of the Weber number smaller than one. In contrast, we have shown here that, in the axisymmetric case, a region of local absolute instability exists near the exit independently of the value of We . However, when non-parallel terms are considered, it has been found that $\omega_{0,i} < 0$, $d\omega_{0,i}(x)/dx > 0$ as $x \rightarrow 0$ independently of We and, therefore, the local instability is always convective near the outlet. Thus, the strongly stabilising effect of non-parallel terms is able to compensate for the reduced convection velocity of disturbances. This fact is clearly seen, for instance, in the positive convective acceleration of the basic flow near the interface, $U_X > 0$, which promotes an enhanced downstream transport of the axial velocity perturbations, $U_X \hat{u}$, when compared to the fully parallel approach and which, in turn, leads to smaller values of $\omega_{0,i}$. Notice that the last conclusion would hold irrespective of the exact shape of the velocity profile, since it relies only on the fact that the free surface accelerates near the outlet due to the substitution of the no-slip condition at the injector wall to a free surface boundary condition.

The formulation used in the present work leads to a natural prediction for the critical Weber number, We_c , below which a global mode is destabilised and subsequently destroys the liquid column leading to a dripping regime. In effect, $\omega_{0,i}(x)$ presents a local maximum inside the jet and, following Pier *et al.* (1998), We_c is defined according to the marginal condition that this maximum be zero. For values of $We > We_c$, the flow is convectively unstable throughout the jet, while, for $We < We_c$, a localised region of absolute

instability takes place in its near field. The function $We_c(Re)$ has been computed for the case without gravity, showing marked differences with respect to the case of a jet with uniform velocity profile considered by Leib & Goldstein (1986*a*). Unfortunately, the available experiments under microgravity conditions were performed either with nozzles (O'Donnell *et al.* 2001; Osborne & Steinberg 2006) or at very small Reynolds numbers (Vihinen *et al.* 1997), thus precluding a comparison with our results. Given the liquid and the value of g , the functional dependence can be alternatively written $We_c(Mo, Bo)$, where Mo is the Morton number, which depends neither on the injector radius nor on the jet velocity, and Bo is the Bond number. The function $We_c(Bo)$, computed here for the particular case of water jets under Earth gravity, provides better agreement with the experiments of Clanet & Lasheras (1999) than previous studies using uniform velocity profiles (Le Dizès 1997; Sauter & Buggisch 2005), thus giving support to the approach used in the present work. It is important to emphasise that, implicit to this approach, is the assumption that the appearance of a pocket of absolute instability leads to the destabilisation of a global mode, independently of the extent of the absolutely unstable domain. Positive evidence for this fact has been given in different contexts, going from model one-dimensional problems (Pier *et al.* 1998) to actual Navier-Stokes flows (see for instance Pier & Huerre 2001; Sevilla & Martínez-Bazán 2004; Lesshafft *et al.* 2006). Finally, let us point out that a more rigorous approach to analyse the flow under consideration would require either using BiGlobal stability analysis (Theofilis 2011), or performing direct numerical simulations. These tasks are left for future work.

Financial support by the Spanish Ministry of Education, Comunidad de Madrid and Universidad Carlos III de Madrid under projects DPI2008-06624-C03-02 and CCG10-UC3M/DPI-4777 is acknowledged. This paper is devoted to the memory of Professor Antonio Barrero, whose integrity will perdure.

REFERENCES

- AMBRAVANESWARAN, B., SUBRAMANI, H. J., PHILLIPS, S. D. & BASARAN, O. A. 2004 Dripping-jetting transitions in a dripping faucet. *Phys. Rev. Lett.* **93**, 034501.
- BARRERO, A. & LOSCERTALES, I. G. 2007 Micro- and nanoparticles via capillary flows. *Annu. Rev. Fluid Mech.* **39**, 89–106.
- BASARAN, O. A. 2002 Small-scale free surface flows with breakup: drop formation and emerging applications. *AIChE J.* **48**, 1842–1848.
- BOGY, D. B. 1979 Drop formation in a circular liquid jet. *Annu. Rev. Fluid Mech.* **11**, 207–228.
- CHOMAZ, J.-M. 2005 Global instabilities in spatially developing flows: Non-normality and nonlinearity. *Ann. Rev. Fluid Mech.* **37**, 357–392.
- CHOMAZ, J.-M., HUERRE, P. & REDEKOPP, L. G. 1988 Bifurcation to local and global modes in spatially developing flows. *Phys. Rev. Lett.* **60**, 25–28.
- CLANET, C. & LASHERAS, J. C. 1999 Transition from dripping to jetting. *J. Fluid Mech.* **383**, 307–326.
- COUAIRO, A. & CHOMAZ, J.-M. 1999 Fully nonlinear global modes in slowly varying flows. *Phys. Fluids* **11**, 3688–3703.
- DEISSLER, R. J. 1987 The convective nature of instability in plane Poiseuille flow. *Phys. Fluids* **30** (8), 2303–2305.
- DUDA, J. L. & VRENTAS, J. S. 1967 Fluid mechanics of laminar liquid jets. *Chem. Eng. Sci.* **22**, 855–869.
- EGGERS, J. 1997 Nonlinear dynamics and breakup of free surface flows. *Rev. Mod. Phys.* **69**, 865–929.
- EGGERS, J. & VILLERMAUX, E. 2008 Physics of liquid jets. *Rep. Prog. Phys.* **71**, 036601.
- GAVIS, J. 1964 Contribution of surface tension to expansion and contraction of capillary jets. *Phys. Fluids* **7** (7), 1097–1098.

- GORDILLO, J. M. & GEKLE, S. 2010 Generation and breakup of Worthington jets after cavity collapse. Part 2: Tip breakup of stretched jets. *J. Fluid Mech.* **663**, 331–346.
- GORDILLO, J. M. & PÉREZ-SABORID, M. 2005 Aerodynamic effects in the break-up of liquid jets: on the first wind-induced break-up regime. *J. Fluid Mech.* **541** (541), 1–20.
- GORDILLO, J. M., PÉREZ-SABORID, M. & GANÁN-CALVO, A. M. 2001 Linear stability of co-flowing liquid–gas jets. *J. Fluid Mech.* **448**, 23–51.
- GOREN, S. L. 1966 Development of the boundary layer at a free surface from a uniform shear flow. *J. Fluid Mech.* **25**, 87–95.
- GOREN, S. L. & WRONSKI, S. 1966 The shape of low-speed capillary jets of Newtonian liquids. *J. Fluid Mech.* **25**, 185–198.
- HARMON, D. B. 1955 Drop sizes from low speed jets. *J. Franklin Inst.* **259** (6), 519 – 522.
- HERBERT, T. 1997 Parabolized stability equations. *Annu. Rev. Fluid Mech.* **29**, 245–283.
- HERRADA, M. A., DEL PINO, C., & FERNÁNDEZ-FERIA, R. 2008 Stability of the boundary layer flow on a long thin rotating cylinder. *Phys. Fluids* **20**, 034105.
- HUERRE, P. & MONKEWITZ, P. 1990 Local and global instabilities in spatially developing flows. *Annu. Rev. Fluid Mech.* **22**, 473–537.
- LE DIZÈS, S. 1997 Global modes in falling capillary jets. *Eur. J. Mech. B/Fluids* **16**, 761–778.
- LEIB, S. J. & GOLDSTEIN, M. E. 1986*a* Convective and absolute instability of a viscous liquid jet. *Phys. Fluids* **29** (4), 952–954.
- LEIB, S. J. & GOLDSTEIN, M. E. 1986*b* The generation of capillary instabilities on a liquid jet. *J. Fluid Mech.* **168**, 479–500.
- LESSHAFFT, L., HUERRE, P., SAGAUT, P. & TERRACOL, M. 2006 Nonlinear global modes in hot jets. *J. Fluid Mech.* **554**, 393–409.
- LIN, S. P. & REITZ, R. D. 1998 Drop and spray formation from a liquid jet. *Annu. Rev. Fluid Mech.* **30**, 85–105.
- MILES, J. W. 1960 The hydrodynamic stability of a thin film of liquid in uniform shearing motion. *J. Fluid Mech.* **8**, 593–610.
- MONKEWITZ, P. A., DAVIS, J., BOJORQUEZ, B. & YU, M.-H. 1988 The breakup of a liquid jet at high Weber number. *Bull. Am. Phys. Soc.* **33**, 2273.
- MONKEWITZ, P. A., HUERRE, P. & CHOMAZ, J.-M. 1993 Global linear stability analysis of weakly non-parallel shear flows. *J. Fluid Mech.* **251**, 1–20.
- OĞUZ, H. 1998 On the relaxation of laminar jets at high Reynolds numbers. *Phys. Fluids* **10** (2), 361–367.
- OĞUZ, H. & PROSPERETTI, A. 1993 Dynamics of bubble growth and detachment from a needle. *J. Fluid Mech.* **257**, 111–145.
- O'DONNELL, B., CHEN, J. N. & LIN, S. P. 2001 Transition from convective to absolute instability in a liquid jet. *Phys. Fluids* **13** (9), 2732–2734.
- OSBORNE, B. P. & STEINBERG, T. A. 2006 An experimental investigation into liquid jetting modes and break-up mechanisms conducted with a new reduced gravity facility. *Microgravity Sci. Technol.* **XVIII** (3/4), 57–61.
- PHILIPPE, C. & DUMARGUE, P. 1991 Etude de l'établissement d'un jet liquide laminaire émergeant d'une conduite cylindrique verticale semi-infinie et soumis à l'influence de la gravité. *ZAMP* **42**, 227–242.
- PIER, B. & HUERRE, P. 2001 Nonlinear self-sustained structures and fronts in spatially developing wake flows. *J. Fluid Mech.* **145**, 145–174.
- PIER, B., HUERRE, P., CHOMAZ, J.-M. & COUAIRON, A. 1998 Steep nonlinear global modes in spatially developing media. *Phys. Fluids* **10** (10), 2433–2435.
- RAYLEIGH, W. S. 1878 On the instability of jets. *Proc. London Math. Soc.* **10**, 4–13.
- SAUTER, U. S. & BUGGISCH, H. W. 2005 Stability of initially slow viscous jets driven by gravity. *J. Fluid Mech.* **533**, 237–257.
- SEVILLA, A., GORDILLO, J. M. & MARTÍNEZ-BAZÁN, C. 2005 Transition from bubbling to jetting in a coaxial air–water jet. *Phys. Fluids* **17**, 018105.
- SEVILLA, A. & MARTÍNEZ-BAZÁN, C. 2004 Vortex shedding in high Reynolds number axisymmetric bluff-body wakes: Local linear instability and global bleed control. *Phys. Fluids* **16**, 3460.
- SMITH, M. K. & DAVIS, S. H. 1982 The instability of sheared liquid layers. *J. Fluid Mech.* **121**, 187–206.

- SMITH, S. W. J. & MOSS, H. 1917 Experiments with mercury jets. *Proc. Roy. Soc. A* **93**, 373–393.
- SÖDERBERG, L. D. 2003 Absolute and convective instability of a relaxational plane liquid jet. *J. Fluid Mech.* **493**, 89–119.
- THEOFILIS, V. 2011 Global linear instability. *Annu. Rev. Fluid Mech.* **43**, 319–352.
- TILLET, J. P. K. 1968 On the laminar flow in a free jet of liquid at high Reynolds number. *J. Fluid Mech.* **32**, 273–292.
- UTADA, A. S., CHU, L.-Y., FERNANDEZ-NIEVES, A., LINK, D. R., HOLTZE, C. & WEITZ, D. A. 2007 Dripping, jetting, drops, and wetting: The magic of microfluidics. *MRS Bull.* **32**, 702–708.
- VIHINEN, I., HONOHAN, A. M. & LIN, S. P. 1997 Image of absolute instability in a liquid jet. *Phys. Fluids* **9** (11), 3117–3119.
- WEBER, C. 1931 On the breakdown of a fluid jet. *Z. Angew. Math. Mech.* **11**, 136–141.
- WILKES, E. D., PHILLIPS, S. D. & BASARAN, O. A. 1999 Computational and experimental analysis of dynamics of drop formation. *Phys. Fluids* **11** (12), 3577–3598.